Title

Mechanically graded granular scaffolds for osteochondral tissue engineering

Journal

Biomaterials Advances, 186

ISSN

2772-9516

Authors

Mierswa, Sabrina C

Wheeler, Erika E

Moya, Monica L

et al.

Publication Date

2026-09-01

DOI

10.1016/j.bioadv.2026.214908

Mechanically Graded Granular Scaffolds for Osteochondral Tissue Engineering

Sabrina C. Mierswa[1,2,3], Erika E. Wheeler[1,2], Monica L. Moya[3], and J. Kent Leach[1,2]

[1]Department of Orthopaedic Surgery, UC Davis Health, Sacramento, CA, 95817 USA
[2]Department of Biomedical Engineering, University of California, Davis, CA, 95616 USA
[3]Engineering Directorate, Lawrence Livermore National Laboratory, Livermore, CA, USA

Running title: MSC osteochondral differentiation in gradient hydrogels

*Corresponding author:
J. Kent Leach, Ph.D.
UC Davis Health
Department of Orthopaedic Surgery
4860 Y Street, Suite 3800
Sacramento, CA 95817
Email: jkleach@health.ucdavis.edu

Author contributions:

SCM: methodology, validation, formal analysis, investigation, writing – manuscript composition and editing

EEW: methodology, investigation, manuscript editing

MLM: conceptualization, resources, writing – manuscript editing, funding, administrative support, supervision

JKL: conceptualization, resources, writing – manuscript editing, funding, administrative support, supervision

Abstract

Engineered scaffolds designed to approximate the mechanical microenvironment of the osteochondral unit often address this complexity using discrete, two-phase architectures that introduce mechanical discontinuities and interfacial stress concentrations rather than a contiguous stiffness transition. To address this challenge, we created a photoannealed polyethylene glycol (PEG) granular scaffold with a spatially controlled stiffness gradient within a cell-permissive, macroporous architecture. Stiffness was dictated by photoannealing microgels using a photomask. We tuned void volume and available surface area by varying microgel diameter and tested how mesenchymal stromal cells (MSCs) interpret local mechanical environments. MSCs exhibited position-dependent differences in morphology, cytoskeletal structure, matrix deposition, and lineage-specific gene expression within the gradient scaffolds. Softer regions supported rounded cell morphology and deposition of a glycosaminoglycan-rich matrix, whereas stiffer regions promoted cell elongation, increased cytoskeletal tension, and expression of mineral-associated markers. Gradients formed from smaller microgels magnified these spatial responses by increasing cellular confinement and adhesion site availability. Disruption of actomyosin contractility eliminated these regional differences, demonstrating that MSCs rely on tension-dependent mechanotransduction to interpret the gradient. These findings reveal that coupling microgel architecture with continuous stiffness transitions provides a tractable platform to study multiscale mechanobiologic regulation and spatially guide osteochondral tissue formation.

Keywords: photocrosslinking, gradient, stiffness, microgels, osteochondral

Introduction

Articular cartilage possesses limited intrinsic repair capacity and progressively degenerates after injury or disease. [1] Although procedures such as autologous chondrocyte implantation (ACI) and its scaffold-based variant, matrix-induced autologous chondrocyte implantation (MACI), as well as graft- or scaffold-based approaches, can provide temporary symptom relief, they rarely restore durable hyaline cartilage or re-establish the structural and mechanical integrity of the osteochondral unit. [2, 3] Successful regeneration of osteochondral tissues requires coordinated repair of cartilage and subchondral bone, which differ markedly in composition, stiffness, and mineral content. [4, 5] In native tissue, the calcified cartilage layer provides a gradual mechanical transition that distributes load across the interface. [6, 7] Biomaterials that recapitulate this continuous gradient, rather than relying on discrete phases, may better capture spatially varying mechanical cues relevant to osteochondral tissue organization and integrated tissue healing. As a result, considerable effort has focused on scaffolds that present controlled mechanical gradients and regionally appropriate microenvironments to guide mesenchymal stromal cell (MSC) differentiation toward chondral or osseous phenotypes. [8-11]

Advances in biomaterial processing enable spatial patterning of material properties with high precision, with hydrogels offering exceptional tunability. Photopolymerization and grayscale photopatterning can generate stiffness gradients spanning physiologic ranges, providing improved control over tissue-relevant mechanics compared to bilayer constructs with abrupt transitions. [12-15] Such gradients regulate MSC morphology, cytoskeletal tension, and lineage commitment in a spatially dependent manner. [14] Macroporous granular scaffolds fabricated from hydrogel microparticles (microgels) provide interconnected void spaces that enhance nutrient transport, enable rapid cell infiltration, and support robust matrix deposition relative to bulk hydrogels. [16-18] Microgel-based systems have achieved increased cartilage matrix formation,

mineralized tissue deposition, and improved osteochondral interface formation compared to single-phase hydrogels. [9, 19, 20] Although microgels can be functionalized to introduce region-specific biochemical cues, most designs remain multiphasic and retain discrete interfaces prone to mechanical mismatch or delamination. [8, 9] These limitations highlight the need for a unified scaffold architecture that integrates a continuous mechanical gradient with the inherent porosity and modularity of microgel assemblies. Therefore, the objective of this study was to develop a microgel-based scaffold with a continuous stiffness gradient to evaluate how spatial mechanical cues and scaffold architecture regulate MSC response in a controlled *in vitro* system.

Here, we report a photopatterned polyethylene glycol (PEG)-based microgel scaffold possessing a continuous compressive modulus gradient (~2–60 kPa) spanning a mechanically relevant range for osteochondral tissues. The scaffold assembles through in situ microgel annealing to form a stable, macroporous architecture that supports MSC infiltration and matrix distribution while eliminating the sharp interfaces inherent to bilayer systems. Prior work leverages lineage-specific inductive peptides to promote zonal osteochondral differentiation in either bulk hydrogels or annealed microgel scaffolds. In contrast, the present study evaluates how the stiffness gradient and microgel-derived porosity guide spatial MSC behavior under a uniform baseline RGD ligand density, thereby decoupling global adhesive support from localized mechanical cues. Specifically, we investigate whether combining a continuous stiffness gradient with a porous, cell-permissive microgel network can induce MSCs toward site-specific lineages and support more coordinated osteochondral regeneration than conventional scaffolds lacking graded mechanical properties. Accordingly, this study was designed as a mechanistic *in vitro* model to isolate the effects of spatial stiffness gradients on MSC behavior rather than to assess osteochondral repair efficacy *in vivo*.

Materials and Methods

MSC expansion and mixed media cell culture

Human bone marrow–derived MSCs were obtained from a single donor (21-year-old male; RoosterBio, Frederick, MD) and used at passages 4–5 for all experiments. MSCs were expanded in Alpha Modified Eagle Medium (αMEM; Invitrogen, Carlsbad, CA) supplemented with 10% v/v fetal bovine serum (FBS; Sigma) and 1% penicillin/streptomycin (P/S; Gemini Bio-Products, Sacramento, CA) at 37°C with 5% CO_2 until reaching confluency. For osteochondral differentiation, constructs were cultured for 21 days at 37°C with 5% CO_2 in a mixed induction medium composed of a 1:1 (v/v) blend of 2× chondrogenic medium and 2× osteogenic medium. The 2× osteogenic medium contained 20 mM β-glycerophosphate, 100 µg/mL ascorbate-2-phosphate, and 20 nM dexamethasone (Sigma Chemical, St. Louis, MO). The 2× chondrogenic medium consisted of Dulbecco's Modified Eagle Medium (DMEM) with 2% P/S, 2 µM dexamethasone, 20 ng/mL TGF-β3, 100 µM ascorbic acid, 80 µg/mL L-proline, 220 µg/mL sodium pyruvate, and ITS supplement containing 20 µg/mL bovine insulin, 11 µg/mL human transferrin, and 13.4 ng/mL selenium (MilliporeSigma, Burlington, MA). Media was changed every 2–3 days.

Microgel fabrication

Microgels were fabricated using a previously designed microfluidic device. [21-23] The aqueous phase consisted of 8-arm 10 kDa poly(ethylene glycol)–vinyl sulfone (PEG-VS; JenKem, Plano, TX) and 3.5 kDa poly(ethylene glycol)–dithiol (PEG-DT; JenKem) dissolved in 0.15 M triethanolamine (TEOA; pH 5.1) buffer. The final microgel concentrations were 6 mM (6% w/v) PEG-VS and 7.2×10^{-3} M PEG-DT. For cell-adhesive microgels, an RGD peptide (Ac-RGDSPGERCG-NH_2; GenScript) was incorporated into the PEG-VS macromer via thiol–ene Michael-type addition prior to microgel fabrication. The oil phase consisted of Novec 7500 Oil supplemented with Picosurf (Sphere Fluidics, Cambridgeshire, UK) at concentrations matched to

the required droplet size: 0.75 wt% Picosurf for small and medium microgels [21] and 0.25 wt% Picosurf for large microgels. To generate discrete microgel size populations, flow rates of the aqueous and oil phases were systematically adjusted to produce three monodisperse diameters: small (~80 µm), medium (~150 µm), and large (~300 µm). After exiting the device, microgels were combined with a solution of 1% v/v triethylamine (TEA, MilliporeSigma) in Novec 7500 Oil using a Y-junction and left at room temperature overnight to ensure complete crosslinking. Microgels were cleaned as described [21] and then imaged with brightfield microscopy (EVOS XL Core, Invitrogen) to determine size distribution and monodispersity.

Measurement of diameter and mechanical testing of microgels

Microgels were pipetted onto a petri dish with a glass bottom and imaged at 10x using an EVOS microscope. Microgel diameter was manually measured using ImageJ with at least 3 fields of view. Individual microgels were examined using a MicroTester (CellScale, Waterloo, ON) by loading onto an anvil in a water bath filled with PBS at pH 7.25. [9, 22] The microgels were compressed over 30 s to 50% of their original diameter by a 2 × 2 mm stainless-steel platen attached to a 0.2032 diameter tungsten rod. The displacement and force of each microgel was recorded and utilized to calculate the modulus. The modulus was calculated from the linear region of the compressive modulus versus the nominal strain graph using a custom Python code.

Fabrication of continuous grayscale photomask

A continuous grayscale photomask was created to generate spatial variations in UV exposure during scaffold annealing as described. [13] The gradient pattern was developed in AutoCAD (Autodesk, San Francisco, CA) by arranging 30-µm diameter dots at 10-µm center-to-center spacing, with dot density modulated to produce incremental changes in opacity. This digital layout was transferred to a flexible Fuji mylar substrate (1.78-mm thick) and fabricated using an

Orbotech LP9008 photoplotter (CAD/Art Services, Bandon, OR). The resulting photomask consisted of an 8 mm × 8 mm patterned region with a continuous grayscale transition.

Encapsulation of MSCs in UV crosslinked system

Human MSCs were pelleted and resuspended in the respective microgel slurry at 5×10^6 cells/mL in 25 mM HEPES containing 0.1% (w/v) lithium phenyl-2,4,6-trimethylbenzoyl-phosphinate (LAP) (Sigma Aldrich) photoinitiator to form a 6% w/v precursor mixture**.** The cell-microgel suspension was pipetted into 8 mm square silicone molds, with 120 µL per mold yielding gels approximately 1.5 mm thick. To generate continuous stiffness gradients, a grayscale photomask was placed directly on top of the gel prior to UV exposure. Gels were crosslinked under 20 mW cm^{-2} UV light (320–500 nm; Omnicure S2000) for 4 min. The lamp output was adjusted so that the most transparent region of the photomask received 20 mW cm^{-2}, as verified using a luminometer; attenuation by the photomask was compensated by increasing the source intensity. For control gels, a transparent film of identical thickness replaced the photomask to provide uniform light attenuation and produce scaffolds with homogeneous crosslinking. After curing, gels were removed from molds and transferred into mixed medium for subsequent experiments.

Determination of biophysical properties of annealed microgel scaffolds

Microgel scaffolds were first assembled by photoannealing PEG-VS/PEG-DT microgels as described above. Annealed microgel scaffolds were placed in 400 µL of 1 mg mL^{-1} of FITC-Dextran (200 kDa, Sigma) overnight at RT. Samples were washed three times with PBS and imaged on a confocal microscope. FITC-Dextran images were used to calculate pore volume and total scaffold volume to determine porosity using IMARIS (Oxford Instruments). [22] To quantify architectural scaling associated with microgel size, the surface-area-to-volume ratio of individual

microgels was calculated assuming spherical geometry using measured microgel diameters. Surface area and volume were estimated using standard geometric relationships for spheres. Relative interfacial surface area within the scaffold was estimated by combining these geometric relationships with experimentally measured scaffold porosity values. These calculations were used to compare the relative surface area available for cell–matrix interactions across scaffolds assembled from small, medium, and large microgels (**Fig. S2**). RGD functionalization of microgels was assessed using a ninhydrin-based amine detection assay. [24] Acellular microgel scaffolds were fabricated with or without photocrosslinking through the photomask, equilibrated in PBS, and incubated with ninhydrin reagent (2%w/v in ethanol; Sigma-Aldrich). Absorbance at 570 nm was used to quantify free amines relative to glycine standards, providing a measure of RGD incorporation normalized to sample wet mass.

Gel mechanical properties were assessed using a Piuma nanoindenter (Optics11, Amsterdam, The Netherlands) equipped with a spherical tip cantilever designed for soft hydrogel testing. Mechanical testing was performed on Day 1 and Day 21 for constructs formed from each microgel diameter and for both gradient and non-gradient conditions. For Day 21 measurements, constructs were maintained under identical culture conditions and indentation mapping was performed at the same spatial positions used for Day 1 testing to enable direct comparison of gradient profiles over time. To stabilize samples during indentation, each gel was partially embedded in 1.5% (w/v) agarose such that the lateral and bottom surfaces were supported while the top surface remained free of contact. Phosphate-buffered saline (PBS) was added to the sample well to maintain hydration throughout testing. Indentation mapping was conducted at room temperature. For gradient constructs, measurements were acquired along the lateral (horizontal) axis across the photopatterned region at 500 μm intervals, and along the vertical axis to confirm the presence and continuity of the stiffness gradient. Non-gradient control gels were tested at matched spatial positions. At each indentation point, the cantilever approached the gel at a

controlled velocity and indented to 5 μm while recording force and displacement. [25, 26] Young's moduli were calculated from the force–indentation curves using the Piuma analysis software, which computes modulus from the indentation slope using proprietary calibration routines appropriate for soft hydrogel materials. Values from each position were recorded and used to generate spatial stiffness maps for all groups. The spatial stiffness gradient was quantified by calculating the change in modulus across the photopatterned region and dividing by the total gradient length (8 mm) to estimate the average gradient slope (kPa/mm).

Degradation of photocrosslinked PEG hydrogels

Acellular bulk gels were stored in 1 mL mixed media and media changed every 2-3 days. Gels were collected after 1, 7, and 21 days and then lyophilized for 3-5 days. The lyophilized mass of hydrogels was measured using a Mettler Toledo XPR2 Microbalance (Mettler-Toledo, Columbus, OH). To assess scaffold hydration over time, acellular microgel scaffolds were collected at Days 0, 1, 7, and 21. Samples were briefly blotted to remove excess surface liquid and weighed to obtain wet mass. Constructs were then lyophilized for 3–5 days and reweighed to determine dry mass. The mass swelling ratio (Q) was calculated as the ratio of wet mass to dry mass for each sample.

Biochemical assays to quantify matrix deposition

Samples collected on Days 1 and 7 were placed in 1X passive lysis buffer (PLB) and sonicated twice to produce homogenates for DNA and glycosaminoglycan (GAG) quantification. Day 21 samples were placed in papain buffer extract (PBE) buffer, sonicated twice, and digested overnight at 60°C in activated papain solution (3.88 U/mL; MilliporeSigma). DNA content at all time points was quantified using the Quant-iT PicoGreen dsDNA Assay Kit (Thermo Fisher Scientific,

Waltham, MA) following the manufacturer's fluorometric protocol. Sulfated GAG content was measured at Days 1, 7, and 21 using a DMMB assay. [9]

Total collagen content at Day 21 was determined by hydroxyproline analysis of the papain digest using chloramine-T oxidation and Ehrlich's reagent–based colorimetric detection calibrated to a hydroxyproline standard curve. Alkaline phosphatase activity was assessed on Day 7 using a p-nitrophenyl phosphate substrate. Calcium content on Day 21 was quantified following extraction in 1 M HCl and subsequent colorimetric analysis.

Interrogation of cell adhesion and spreading within gradient scaffolds

Samples collected on Days 1, 7, and 21 were fixed in 4% paraformaldehyde (PFA) for 1 h at room temperature and washed twice with PBS. Constructs were then incubated with AlexaFluor 488–conjugated phalloidin (1:400; Invitrogen, A12379) and DAPI (1:500; Invitrogen) for 1 h at room temperature. After staining, samples were washed three times with PBS and imaged using a Leica Stellaris 5 confocal microscope (Leica Microsystems, Wetzlar, Germany).

Lineage specific gene expression analysis via qRT-PCR

Samples were collected in TRIzol Reagent (Invitrogen) for PCR analysis according to the manufacturer's protocol. Total RNA was isolated, and 800 ng of RNA was reverse transcribed using the QuantiTect Reverse Transcription Kit (QIAGEN, Valencia, CA) and normalized to a final concentration of 10 ng/µL. RNA purity and concentration were verified using a Nanodrop One spectrophotometer (Thermo Fisher Scientific, Waltham, MA). Quantitative real-time PCR was performed using the QuantiFast Probe PCR Kit (QIAGEN) on a QuantStudio 6 system (Applied Biosystems, Waltham, MA). TaqMan primers and probes for *GAPDH* (Hs_02786624_g1), *COL1A1* (Hs00164004_m1), *RUNX2* (Hs), and *BGLAP* (Hs) were obtained from Thermo Fisher Scientific. Thermal cycling conditions consisted of an initial denaturation at 95 °C for 3 min,

followed by 45 cycles of 95 °C for 3 s and 60 °C for 30 s. Gene expression was normalized to *GAPDH* to obtain ΔCt values. Fold changes relative to Day 0 MSCs were determined using the 2^−ΔΔCt method.

For spatial gene expression analysis, each 8 mm × 8 mm construct was sectioned into four equal zones along the gradient axis at Day 7. Gels were removed from culture, rinsed briefly in PBS, and cut into four ~2-mm strips using a sterile scalpel while maintaining soft-to-stiff orientation. Each strip was immediately transferred into TRIzol and processed independently for RNA isolation and subsequent qPCR.

Histological staining

After 21 days in mixed media and standard culture conditions, samples were fixed in 4% paraformaldehyde (PFA) for 1 h, washed twice with PBS, then embedded in Tissuetek OCT compound. Samples were snap-frozen, sectioned at 7 µm using a cryostat, and mounted onto charged slides. Sections were stained with Safranin O and counterstained with Fast Green to assess GAG deposition using standard protocols, followed by Alizarin Red staining on adjacent sections to evaluate mineralization. Images were acquired immediately after staining with brightfield microscopy using an EVOS XL Core.

Determining mechanosensitivity of entrapped MSCs

To evaluate MSC mechanosensitivity, microgel constructs were cultured in mixed differentiation medium supplemented with 10 µM blebbistatin (Sigma-Aldrich) for 7 days, with medium exchanged every 48 h and protected from light. At day 7, samples were collected in TRIzol Reagent (Invitrogen) for gene expression analysis. Total RNA was isolated and reverse transcribed as described above. Quantitative real-time PCR was performed on a QuantStudio 6

system (Applied Biosystems). TaqMan probes for *CYR61* (Hs), *CTGF* (Hs), and *GAPDH* (Hs) were obtained from Thermo Fisher Scientific. Expression levels were normalized to GAPDH (ΔCt), and fold-changes were determined using the 2^−ΔΔCt method.

For cytoskeletal analysis, parallel constructs were fixed in 4% paraformaldehyde and stained with Alexa Fluor–conjugated phalloidin (F-actin) and DAPI (nuclei). Stained constructs were washed and imaged by confocal microscopy to assess F-actin organization and cell morphology under contractility inhibition.

Statistical analysis

Data are presented as means ± standard deviation. Statistical analysis was performed using GraphPad Prism 10 software (GraphPad Software, San Diego, CA) using one-way or two-way ANOVA with Tukey's multiple comparisons test or Student's t-test when appropriate. All data were tested for normality using the Shapiro-Wilk normality test. Differences were considered statistically significant at $p \leq 0.05$. Statistical differences between groups in figures are indicated by letter annotations or "ns" where differences were not significant. Groups that are significantly different are denoted with different letters, while groups that share letters are statistically similar.

Results

Microgel fabrication yields monodisperse PEG microgels

Microgels were fabricated by droplet microfluidics using PicoSurf-stabilized water-in-oil emulsions and then crosslinked to generate three microgel populations with distinct diameters (**Fig. 1A**). This process reproducibly produced small (~80 µm), medium (~150 µm), and large (~300 µm) microgels (**Fig. 1B**) that possessed the expected size hierarchy when visualized by brightfield microscopy (**Fig. 1C**). Quantitative size analysis confirmed narrow distributions for all

groups, with coefficients of variation below ~12% (**Fig. 1D**). Mechanical testing of individual microgels revealed comparable compressive moduli across all size groups (~30-35 kPa), with no statistically significant differences between small, medium, and large microgels (**Fig. 1E**). Although individual microgels exhibited compressive moduli of ~30–35 kPa, nanoindentation measurements of the assembled scaffold reflect the apparent modulus of the porous microgel network, which includes contributions from void space and interparticle interfaces rather than the intrinsic modulus of isolated microgels. Together, these data demonstrate that the fabrication approach yields monodisperse PEG microgels with reproducible diameters and comparable compressive moduli across size groups.

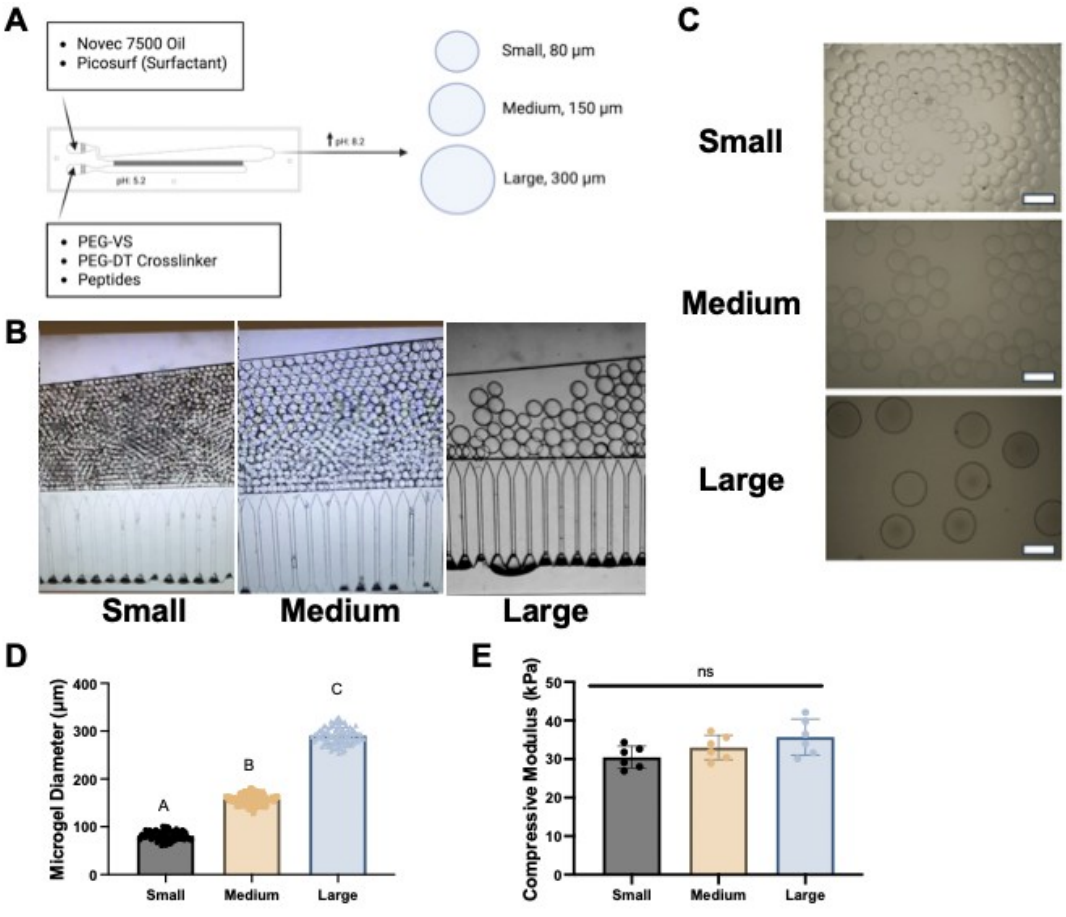

Figure 1. Fabrication and characterization of PEG microgels with defined diameters. (A) Schematic of the microfluidic droplet generation platform used to fabricate PEG-VS/PEG-DT

microgels of defined diameters (Small: ~80 µm, Medium: ~150 µm, Large: ~300 µm). **(B)** Representative brightfield images of the microfluidic devices illustrate the scaling of droplet size with increasing channel height. **(C)** Brightfield micrographs of the resulting microgel populations confirm uniform morphology and distinct size distributions for small, medium, and large groups. Scale bars represent 200 µm. **(D)** Quantification of microgel diameter for each population shows narrow size distributions with coefficients of variation <12%, indicating successful generation of monodisperse microgels (n = 50 microgels per group). **(E)** Compressive testing of individual microgels revealed no statistically significant differences in modulus across size groups. Data are presented as mean ± SD (n = 6). Statistical significance was determined using one-way ANOVA with Tukey's multiple comparisons test where appropriate. Groups that do not share a letter are significantly different ($p < 0.05$); ns = not significant.

Mechanical and structural properties of photoannealed microgel scaffolds

Microgel scaffolds fabricated using small, medium, and large microgels were photoannealed under a grayscale photomask to generate constructs with distinct void architectures and spatially patterned mechanical properties (**Fig. 2A**). Unconfined Piuma nanoindentation performed across the scaffold surface along the 8-mm scaffold length demonstrated that scaffolds assembled from all microgel sizes displayed a monotonic increase in compressive modulus along the length of the photopatterned region, confirming formation of a continuous linear stiffness gradient (**Fig. 2B**). Across the 8-mm photopatterned region, modulus increased from ~2–5 kPa in the softest regions to ~50–60 kPa in the stiffest regions, corresponding to an average gradient slope of ~6–7 kPa/mm at Day 1. This spatial mechanical transition was preserved at Day 21, confirming stability of the gradient across the culture period. In contrast, scaffolds annealed without a photomask displayed uniform mechanical properties along

the scaffold length. Comparison of Day 1 bulk compressive moduli across microgel sizes revealed no significant differences between photomask-annealed and non-photomask controls for any size, indicating that gradient formation did not alter overall scaffold stiffness (**Fig. 2C**).

Confocal z-stacks revealed size-dependent void architecture, with small microgels resulting in scaffolds with tightly packed pores, medium microgels forming intermediate void networks, and large microgels yielding visibly enlarged and more heterogeneous pores (**Fig. 2D**). Quantification of scaffold porosity showed that large-microgel scaffolds exhibited significantly higher porosity compared to small and medium groups, while the latter two did not differ from one another (**Fig. 2E**). To further quantify architectural differences between scaffold types, we calculated the surface-area-to-volume ratio associated with each microgel size and estimated the relative interfacial surface area within the scaffold using experimentally measured porosity values (**Fig. S2**). These geometric analyses confirmed that decreasing microgel diameter increases scaffold surface area relative to volume and estimated interfacial contact area within the construct. To evaluate scaffold stability over time, dry mass, swelling ratio, and compressive modulus were measured over 21 days. Dry mass remained unchanged through Day 21, indicating stable polymer content and minimal degradation of the PEG network over the culture duration (**Fig. 2F**). RGD incorporation was confirmed by ninhydrin-based amine quantification; as expected, peptide loading did not differ between scaffold sizes (*data not shown*). Bulk compressive modulus measured at Day 21 did not significantly differ from Day 1 and was also unchanged between scaffolds assembled regardless of photomask (**Fig. 2G**). Similarly, swelling ratios were stable across timepoints, demonstrating consistent scaffold hydration throughout the culture period (**Fig. 2H**). Together, these measurements indicate that the PEG-VS/PEG-DT scaffold maintained structural and mechanical stability throughout the 21-day culture period. Nanoindentation measurements performed at Day 21 demonstrated that stiffness gradients were preserved across

all scaffold architectures, with modulus increasing progressively along the scaffold length for small, medium, and large microgel constructs (**Fig. 2I**). Although measured modulus values were slightly lower than those observed at Day 1, the spatial gradient and relative ordering of scaffold architectures (small > medium > large) were preserved, confirming the persistence of the photopatterned mechanical profile over time.

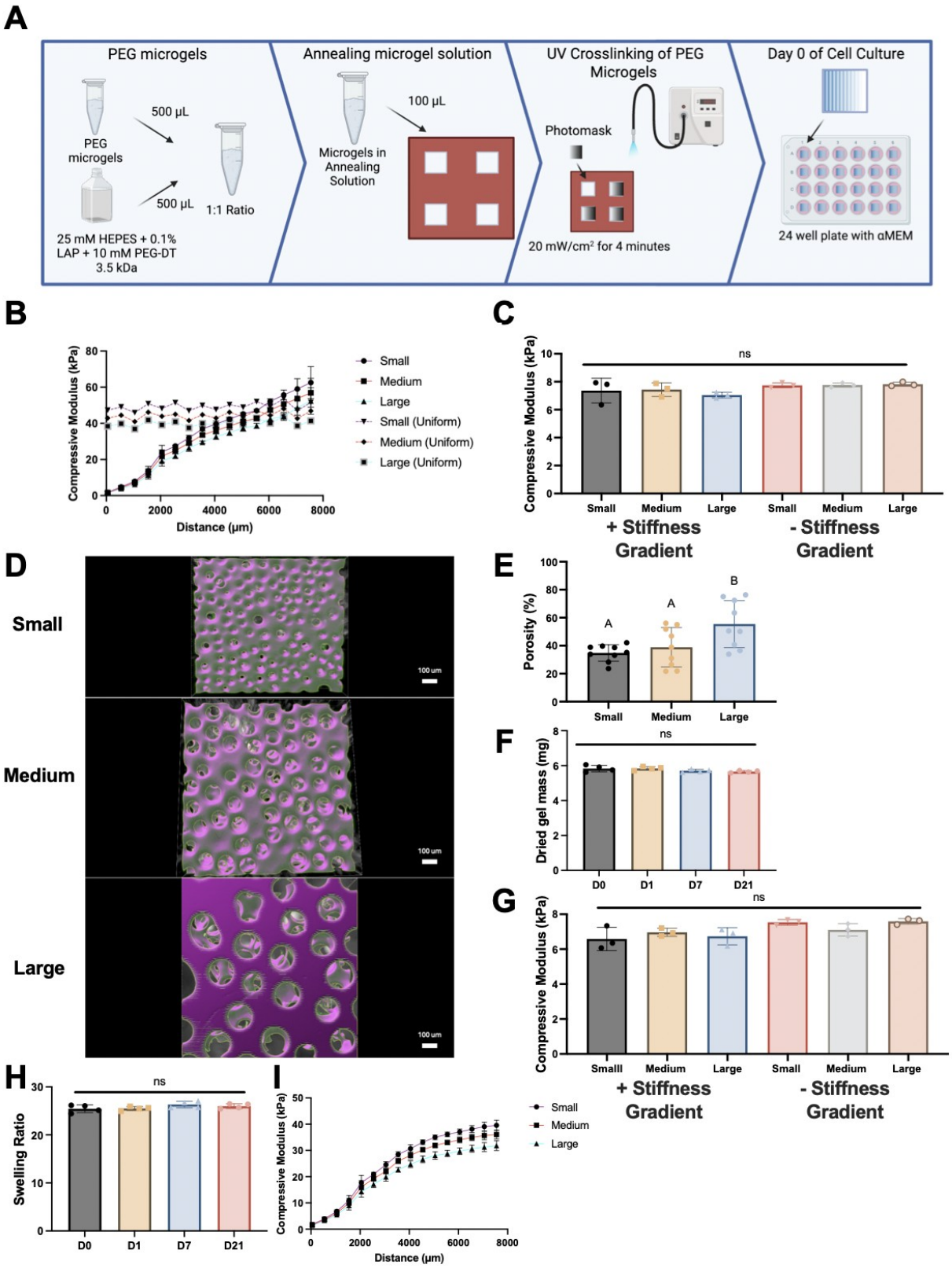
A
PEG microgels
500 µL
PEG microgels
500 µL
1:1 Ratio
25 mM HEPES + 0.1% LAP + 10 mM PEG-DT 3.5 kDa
Annealing microgel solution
100 µL
Microgels in Annealing Solution
UV Crosslinking of PEG Microgels
Photomask
20 mW/cm² for 4 minutes
Day 0 of Cell Culture
24 well plate with αMEM
B
Compressive Modulus (kPa)
Distance (µm)
Small
Medium
Large
Small (Uniform)
Medium (Uniform)
Large (Uniform)
C
Compressive Modulus (kPa)
ns
Small
Medium
Large
Small
Medium
Large
+ Stiffness Gradient
- Stiffness Gradient
D
Small
Medium
Large
100 um
E
Porosity (%)
A
A
B
Small
Medium
Large
F
Dried gel mass (mg)
ns
D0
D1
D7
D21
G
Compressive Modulus (kPa)
ns
Smalll
Medium
Large
Small
Medium
Large
+ Stiffness Gradient
- Stiffness Gradient
Small
Medium
Large
H
Swelling Ratio
ns
D0
D1
D7
D21
I
Compressive Modulus (kPa)
Distance (µm)

Figure 2. Mechanical and structural characterization of photoannealed microgel scaffolds. **(A)** Schematic of microgel annealing and photomask-mediated crosslinking workflow. **(B)** Compressive modulus measured by Piuma nanoindentation across the 8-mm scaffold length (0-8000 μm) for small, medium, and large microgel scaffolds on Day 1. **(C)** Comparison of Day 1 compressive moduli for constructs annealed with or without a photomask. **(D)** Representative confocal reconstructions of pore architecture from the middle/central region for small, medium, and large microgel scaffolds. Dextran fluorescence was used as a space-filling tracer to visualize void architecture. Differences in signal intensity reflect pore geometry and optical path length rather than concentration. Scale bars represent 200 μm. **(E)** Quantified porosity (%) across microgel sizes reveals significantly increased porosity in large-microgel constructs. **(F)** Dry mass of scaffolds measured at Days 0, 1, 7, and 21 demonstrates stable polymer content over time. (**G**) Bulk compressive modulus measured on Day 21 for scaffolds assembled with (+ stiffness gradient) or without (– stiffness gradient) photomask-mediated crosslinking. (**H**) Mass swelling ratio of photomask-annealed scaffolds measured at Days 0, 1, 7, and 21 showing stable hydration over time. (**I**) Compressive modulus measured by nanoindentation across the scaffold length on Day 21 confirming persistence of the stiffness gradient across microgel sizes. Data are presented as mean ± SD (n = 3–6). Statistical significance was determined using one-way or two-way ANOVA with Tukey's multiple comparisons test where appropriate. Groups that do not share a letter are significantly different ($p < 0.05$); ns = not significant.

MSCs exhibit stiffness-dependent morphology and early matrix production in gradient macroporous scaffolds

As illustrated in **Fig. 3A**, PEG microgels were fabricated and encapsulated with MSCs, photoannealed through a grayscale mask to establish the stiffness gradient and cultured for 7 days in mixed osteochondral medium to assess spatially dependent cellular responses. Following culture, constructs were sectioned into four discrete sections – Soft, Mid-Soft, Mid-Stiff, and Stiff – for spatially resolved analysis (**Fig. 3B**). Stiffness-dependent transcriptional responses were evident by Day 7. Relative expression of *SOX9*, *COL1A1*, *RUNX2* varied across stiffness regions and depended on microgel size (**Fig. 3C**). In small and medium microgels, *SOX9* expression was highest in the Mid-Soft region and diminished in stiffer regions, consistent with enhanced chondrogenic signaling in more compliant environments. In contrast, *COL1A1* and *RUNX2* expression increased with stiffness, reaching highest levels in Mid-Stiff and Stiff regions. Large microgels exhibited attenuated spatial patterning of gene expression, with minimal differences across stiffness regions.

Early matrix deposition mirrored these transcriptional trends. GAG/DNA measured at Day 7 was higher in Soft and Mid-Soft regions for small and medium microgels, indicating preferential early GAG accumulation in compliant regions of the gradient (**Fig. 3D**). In contrast, ALP/DNA activity, an early marker of osteogenic differentiation, increased with stiffness and peaked in Mid-Stiff and Stiff regions for small and medium microgels at Day 7 (**Fig. 3E**). Large microgels again displayed stiffness-dependent variation in both GAG/DNA and ALP/DNA, although the magnitude of differences was diminished compared to scaffolds formed from smaller microgels.

Together, these data demonstrate that microgel-based stiffness gradients enable spatial control over MSC fate decisions at early time points, with softer regions favoring chondrogenic-associated responses and stiffer regions promoting early osteogenic signaling. The diminished spatial sensitivity observed in large microgels suggests that void architecture and microgel size modulate how MSCs interpret local mechanical cues within gradient scaffolds.

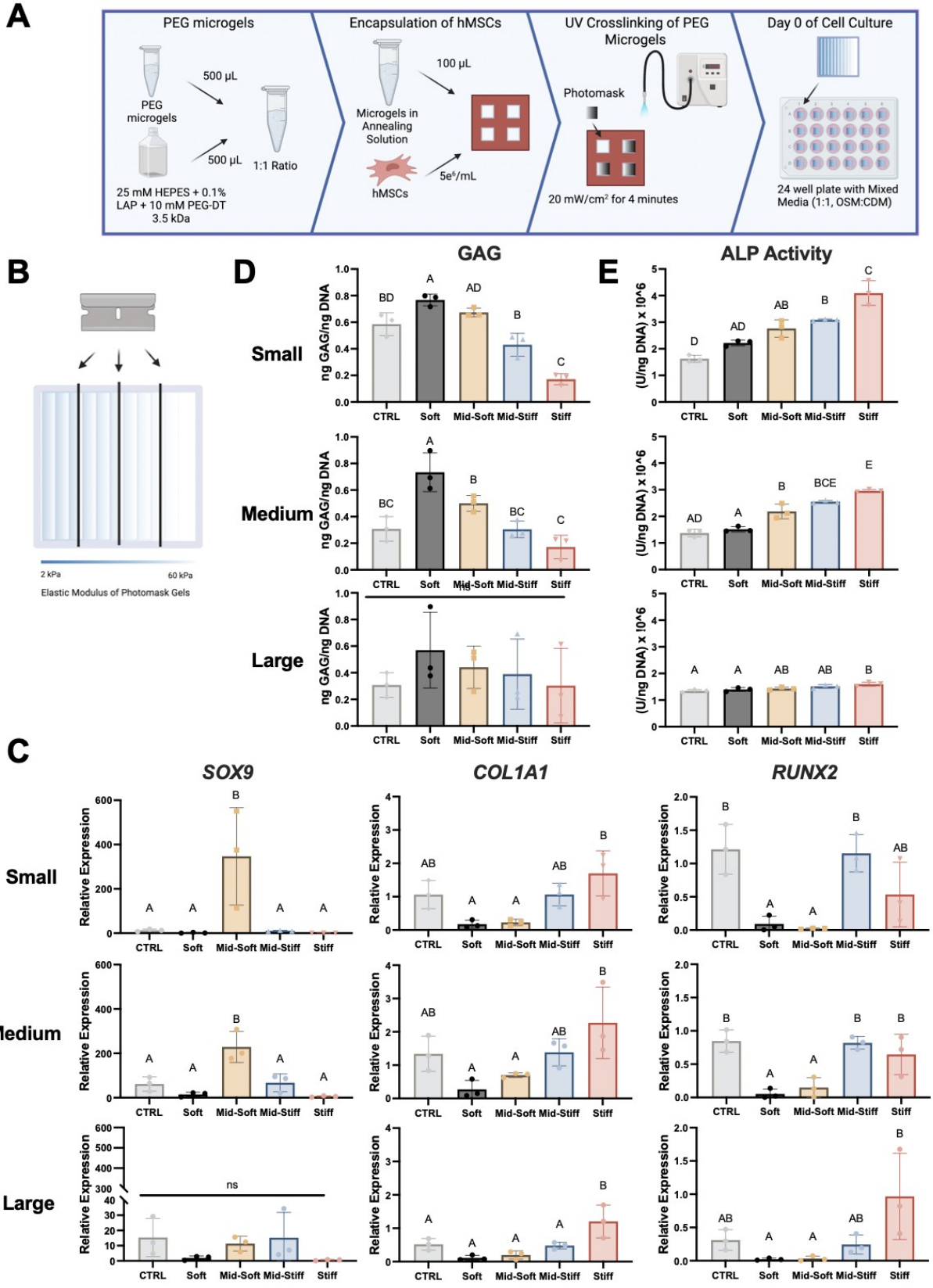
A
PEG microgels
500 µL
PEG microgels
500 µL
1:1 Ratio
25 mM HEPES + 0.1% LAP + 10 mM PEG-DT 3.5 kDa
Encapsulation of hMSCs
100 µL
Microgels in Annealing Solution
5e6/mL
hMSCs
UV Crosslinking of PEG Microgels
Photomask
20 mW/cm2 for 4 minutes
Day 0 of Cell Culture
24 well plate with Mixed Media (1:1, OSM:CDM)
B
2 kPa
60 kPa
Elastic Modulus of Photomask Gels
D
GAG
ng GAG/ng DNA
Small
Medium
Large
CTRL
Soft
Mid-Soft
Mid-Stiff
Stiff
ns
E
ALP Activity
(U/ng DNA) x 10^6
C
SOX9
COL1A1
RUNX2
Relative Expression

Figure 3. MSC gene expression and matrix-related activity across microgel stiffness gradients. (A) Schematic illustrating microgel fabrication, MSC encapsulation, light-mediated gradient formation, and 7 days of culture in mixed media. **(B)** Schematic illustrating sectioning of the photoannealed scaffold into four regions corresponding to Soft, Mid-Soft, Mid-Stiff, and Stiff stiffness zones. **(C)** Relative gene expression of *SOX9*, *COL1A1*, and *RUNX2*; **(D)** GAG/DNA measured; and **(E)** ALP/DNA, all measured at Day 7 across stiffness regions for small, medium, and large microgels. Data are presented as mean ± SD (n = 3). Statistical significance was determined using a one-way ANOVA with Tukey's multiple comparisons test where appropriate. Groups that do not share a letter are significantly different ($p < 0.05$); ns = not significant.

Scaffold-directed zonal ECM deposition along the stiffness gradient

After 21 days, fluorescence imaging revealed pronounced size- and stiffness-dependent cellular organization in small and medium microgel scaffolds, whereas large microgel constructs exhibited reduced spatial organization and diminished zonal patterning (**Fig. 4A**). Stiffness gradient microgel scaffolds exhibited size-dependent spatial patterning of extracellular matrix deposition. In small (80 μm) and medium (150 μm) microgel scaffolds, sulfated proteoglycan accumulation was highest in the Soft and Mid-Soft regions, as indicated by increased GAG/DNA content and corresponding biochemical measurements, and decreased toward the stiffer regions of the gradient (**Fig. 4C**). In contrast, calcium content was elevated in the Mid-Stiff and Stiff regions for both small and medium microgel scaffolds, consistent with stiffness-dependent mineral deposition (**Fig. 4B**). Collagen accumulation followed a similar spatial trend to GAG deposition, with increased collagen/DNA in softer regions and reduced levels in stiffer regions for small and

medium microgels (**Fig. 4D**). In large (300 µm) microgel scaffolds, biochemical measures of calcium, GAG, and collagen revealed no significant differences across gradient regions, indicating

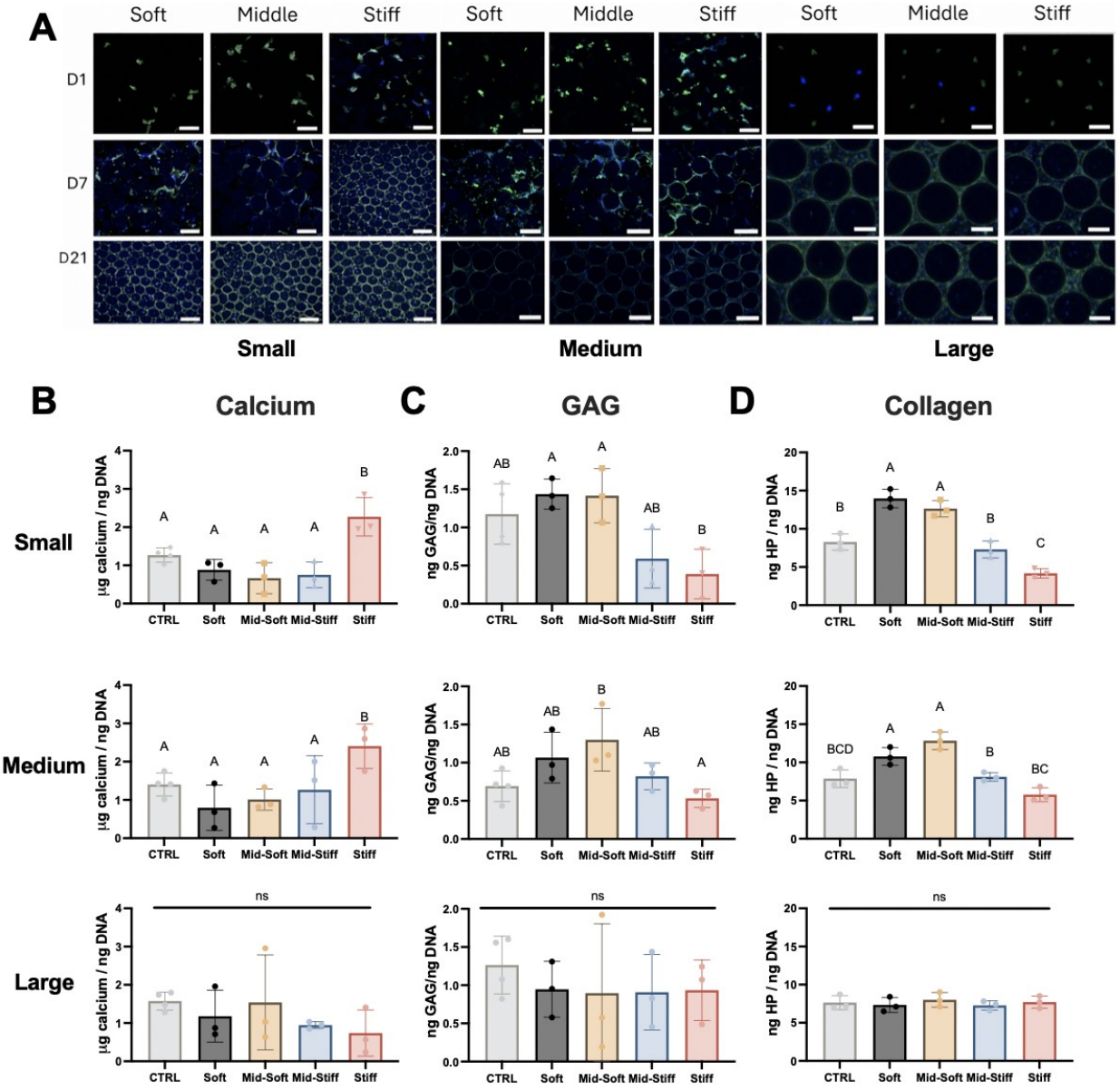

Figure 4. Size-dependent effects of microgel architecture on zonal matrix deposition in stiffness gradient scaffolds. (A) Representative fluorescence images of MSC-laden gradient scaffolds assembled from small (80 µm), medium (150 µm), and large (300 µm) microgels after 21 days. Actin (phalloidin, green) and nuclei (DAPI, blue) demonstrate differences in cellular organization across microgel sizes and stiffness regions. Scale bars = 200 µm. **(B–D)** Biochemical

quantification of calcium deposition normalized to DNA content; (**B**) sulfated glycosaminoglycan (GAG) content normalized to DNA; and (**C**) and collagen (hydroxyproline, HP) content normalized to DNA (**D**) across gradient regions. Data are presented as mean ± SD (n = 3). Statistical significance was determined using one-way ANOVA with Tukey's multiple comparisons test where appropriate. Groups that do not share a letter are significantly different ($p < 0.05$); ns = not significant.

an attenuation of stiffness-dependent matrix patterning with increasing microgel size (**Fig. 4B–D**). Together, these results demonstrate that microgel size modulates the ability of stiffness gradients to spatially direct matrix deposition, with small and medium microgel scaffolds supporting the emergence of distinct cartilage-like (proteoglycan- and collagen-rich) and bone-like (mineral-rich) regions by day 21.

Stiffness-dependent matrix deposition within microgel gradient scaffolds

By day 21, histological staining revealed spatially patterned matrix deposition along the stiffness gradient. Safranin-O/Fast Green staining demonstrated proteoglycan-rich matrix localized predominantly to the soft end of the gradient, with staining intensity decreasing toward the stiff end (**Fig. 5A**). In contrast, Alizarin Red staining showed mineral deposition concentrated at the stiff end of the gradient, whereas minimal mineral staining was observed in the soft regions (**Fig. 5B**). Together, these complementary distributions indicate that scaffold stiffness spatially regulates the cartilage-like and bone-like matrix deposition within the construct. Consistent staining patterns were observed across independent constructs, indicating reproducible spatial regulation of matrix deposition along the gradient. Regions enriched in Safranin-O staining

exhibited limited Alizarin Red signal, whereas regions with strong mineral staining showed reduced proteoglycan content, suggesting mutually exclusive matrix profiles at opposing ends of the stiffness gradient. Together, these histological findings support the emergence of distinct matrix domains within the scaffold by day 21.

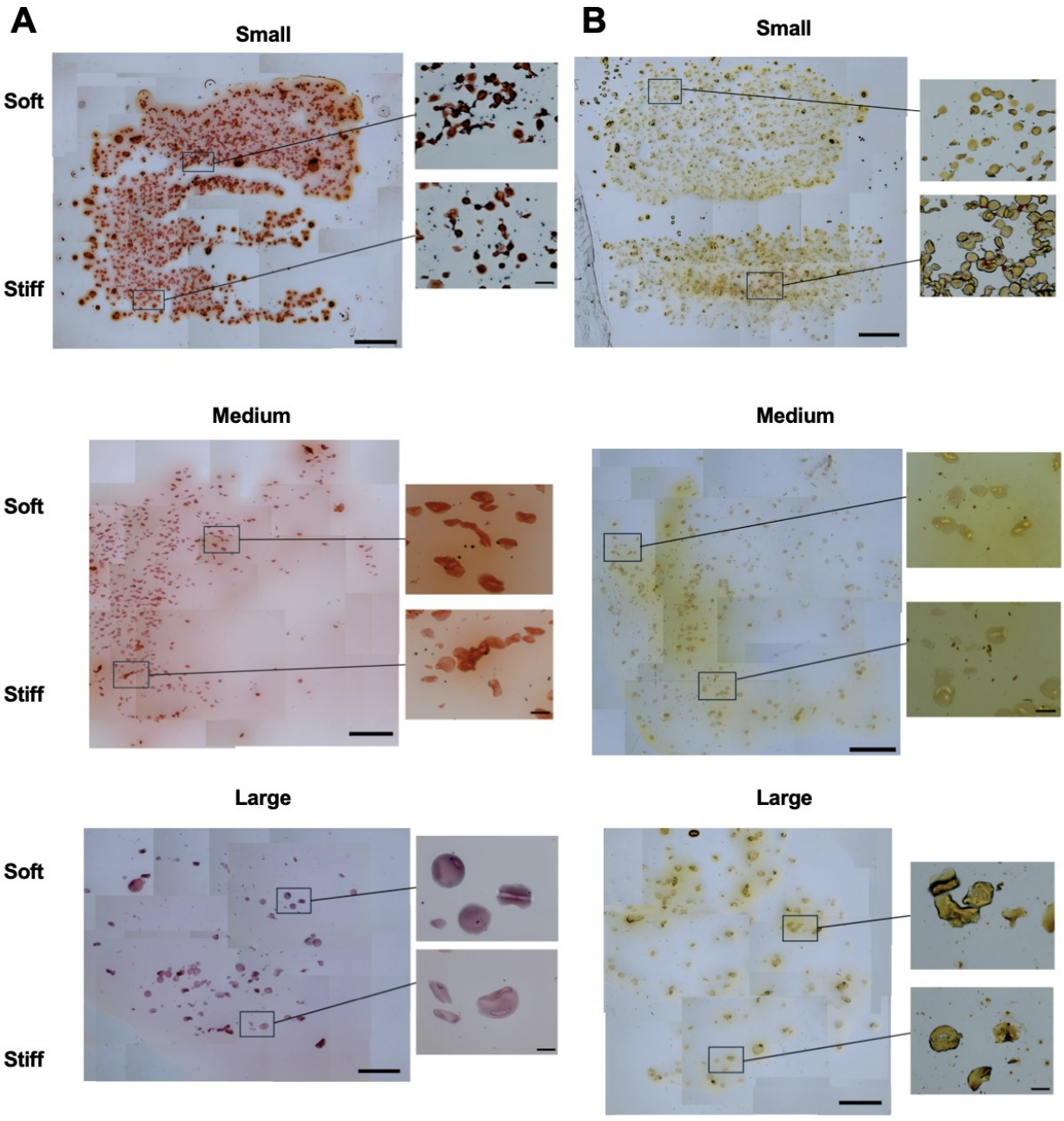

Figure 5. Stiffness-dependent osteochondral matrix deposition in microgel gradient scaffolds. (A) Representative Safranin-O/Fast Green-stained sections of stiffness gradient scaffolds assembled from small (80 μm), medium (150 μm), and large (300 μm) microgels at Day 21. Proteoglycan-rich matrix (Safranin O, red) is enriched toward the soft end of the gradient in small and medium scaffolds, with reduced spatial contrast in large microgel scaffolds. **(B**) Representative Alizarin Red S-stained sections of the same constructs, highlighting calcium-rich mineral deposition (red) preferentially localized to the stiff end of the gradient in small and medium microgel scaffolds, with more uniform staining in large microgel scaffolds. PEG microgels do not retain Alizarin Red S staining and therefore appear unstained, providing contrast between the polymer phase and mineralized regions. Macro-scale images show the full stiffness gradient (scale bars = 1 mm); boxed regions are shown at high magnification (scale bars = 100 μm).

MSC organization and lineage-specific differentiation is dependent on cytoskeletal contraction

We treated constructs with blebbistatin and assessed cytoskeletal organization and mechanosensitive gene expression. DAPI/Phalloidin staining of blebbistatin-treated gradients revealed a uniform reduction in cytoskeletal organization across all regions. Cells appeared more rounded with diminished F-actin organization and exhibited reduced cell spreading (**Fig. 6A**), lacking the well-defined actin structures previously observed in untreated gradient regions (**Fig. 4A**). Even in regions that exhibited extensive spreading in untreated gradients (Mid-Soft and Mid-Stiff), cells displayed minimal elongation and failed to form actin bridges across adjacent microgels. These observations indicate that cytoskeletal contractility is essential for the stiffness-dependent organization observed in untreated constructs**.**

In untreated constructs, *CTGF* expression was spatially patterned across the gradient, with highest expression in regions composed of small microgels and lowest expression in large microgel regions, consistent with stiffness-dependent mechanosensing (**Fig. 6B**). Blebbistatin treatment significantly reduced *CTGF* expression and reduced gradient-dependent differences in small and medium microgel scaffolds, resulting in a collapse of gradient-dependent transcriptional patterning. In large microgel scaffolds, *CTGF* expression was reduced but did not reach statistical significance, consistent with attenuated mechanosensitive signaling in less confined architectures. Together, these data indicate that actomyosin-generated cytoskeletal tension is required for expression of Hippo/YAP-associated transcriptional output in this system and for the graded lineage signaling observed in intact microgel gradients.

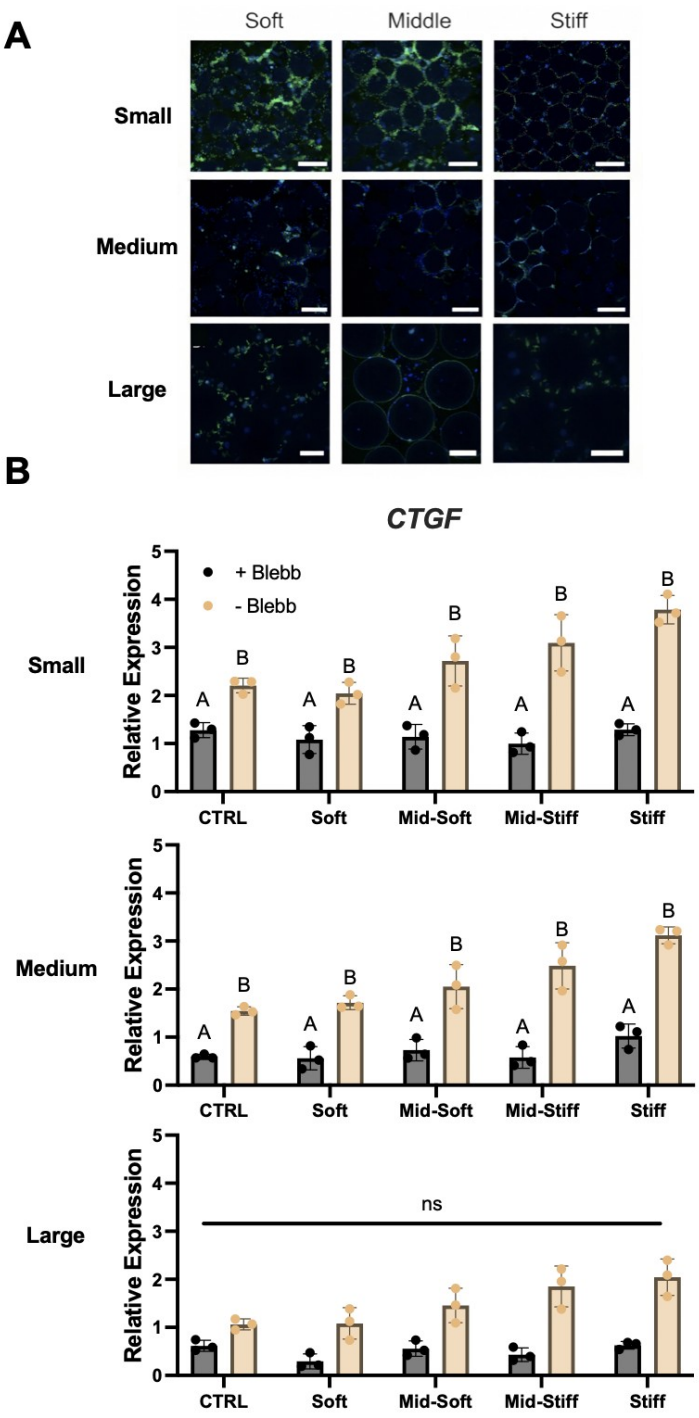

Figure 6. Inhibition of cytoskeletal contractility disrupts gradient-dependent MSC organization and mechanosensitive gene expression. (A) Representative fluorescence images of MSCs in stiffness gradient microgel scaffolds and treated with blebbistatin at Day 7.

Nuclei (DAPI, blue) and F-actin (phalloidin, green) illustrate differences in cellular morphology and cytoskeletal organization across stiffness regions. Scale bars = 200 μm. **(B)** Relative expression of *CTGF* across stiffness gradient regions (Soft, Mid-Soft, Mid-Stiff, Stiff) at Day 7 in the presence (+Blebb) or absence (-Blebb) of blebbistatin. Data are presented as mean ± SD (n = 3 constructs per region). Statistical significance was determined using a Student's t-test where appropriate. Groups that do not share a letter are significantly different ($p < 0.05$); ns = not significant.

Discussion

Engineering scaffolds that recapitulate the continuous mechanical transitions of native osteochondral tissue remains challenging, as most platforms rely on discrete layers or region-specific biochemical patterning that obscure the role of mechanics. To address this limitation, we developed a macroporous microgel scaffold with a continuous stiffness gradient and uniform adhesive cue presentation to isolate the effects of spatially varying mechanics and microstructure on MSC behavior within a single construct. Our data show that a continuous stiffness gradient within a macroporous microgel scaffold elicits clear, region-specific MSC responses that align with local modulus and microstructure. MSCs organized into distinct zones of spreading, matrix production, and lineage gene expression that aligned with the position-dependent mechanical environment. Small and medium microgels created tighter void networks and larger effective surface area, which are consistent with enhanced cell-matrix interactions and amplified these spatial differences. Geometric analysis confirmed that decreasing microgel diameter increases scaffold surface-area-to-volume ratio and estimated interfacial surface area within the construct (**Fig. S2**). Within softer regions, MSCs exhibited more rounded cellular organization and secreted a GAG-rich matrix, whereas stiffer regions induced more spread actin organization, increased cytoskeletal tension, and mineral-associated gene expression. These findings agree with prior

reports showing that MSCs integrate local stiffness and pore geometry to regulate shape, tension generation, and transcriptional programs. [16, 24, 27] By providing a continuous mechanical transition within a single, cell-permissive material, our platform addresses key limitations of bilayer or biphasic scaffolds. Engineered scaffolds designed to approximate the mechanical microenvironment of the osteochondral unit often utilize discrete, biphasic architectures that introduce mechanical discontinuities and interfacial stress concentrations, whereas continuous gradient systems provide a spatially smooth transition in stiffness. By maintaining uniform RGD presentation and eliminating region-specific biochemical cues, the system isolates the contribution of mechanics and pore structure to MSC fate decisions, allowing us to attribute the observed spatial responses directly to physical rather than biochemical patterning. Although pore geometry can influence mass transport, the spatial responses observed here tracked with local stiffness and microgel size rather than construct position, suggesting that differences in diffusion alone are unlikely to account for the observed patterning.

The gradient-dependent outcomes may reflect how MSCs couple cytoskeletal tension with accessible pore geometry, as cells generate higher traction forces when confined within smaller, more interconnected pore networks. [16] In regions formed from small and medium microgels, cells engaged more microgel interfaces and produced greater actomyosin tension, which supported organized F-actin networks and enhanced sensitivity to modest changes in local stiffness. [28, 29] This microstructure-mechanics interaction may explain why these constructs produced sharper transitions in *SOX9, RUNX2,* and *COL1A1* expression, with corresponding stiffness-dependent regulation of the late osteogenic marker *BGLAP* expression, alongside early chondrogenic (*ACAN*) and mechanosensitive (*CYR61*) responses (**Fig. S1**). Because microgel size simultaneously alters pore geometry, void volume, and effective interfacial surface area, these architectural features cannot be fully decoupled in the present system, and the observed

responses should therefore be interpreted as reflecting combined effects of stiffness gradients and scaffold architecture. Larger pores reduced available adhesion sites and lowered effective confinement, likely reducing the forces required to activate tension-sensitive mechanotransduction pathways that drive spatial lineage selection. [30] These findings should therefore be interpreted as reflecting combined influences of scaffold architecture and stiffness gradients rather than stiffness alone. Prior studies show that MSCs depend on these physical cues to modulate YAP/TAZ-associated mechanotransduction signaling and regulate osteochondral fate decisions [31-33]. Our findings extend these principles into a three-dimensional granular scaffold, where pore-scale geometry amplifies or attenuates the ability of cells to interpret continuous stiffness gradients. By aligning microstructure with mechanical transitions, the system creates a context favoring tension-mediated mechanosensing over reliance on exogenous biochemical patterning. [34, 35] While this study focused on osteochondral patterning, the ability to decouple mechanical gradients from biochemical cues within a macroporous scaffold may be broadly applicable to other graded tissue interfaces. Traditional osteochondral scaffold strategies frequently employ biphasic or multilayer designs in which discrete cartilage-like and bone-like materials are combined within a single construct. While these systems enable region-specific biochemical or mechanical properties, the abrupt mechanical transitions created at layer interfaces can introduce local stress concentrations and discontinuities in cell-instructive mechanical cues. Continuous gradients, in contrast, provide a smoother mechanical transition that more closely resembles the progressive modulus changes present in native osteochondral tissue. Previous studies using layered PEG or granular scaffold systems have demonstrated the feasibility of biphasic designs for guiding osteochondral differentiation, including PEG-based granular scaffolds with spatially patterned biochemical cues. [9] However, these systems typically rely on discrete transitions rather than continuous mechanical gradients. Prior work from our group and others have demonstrated that

biphasic or layered microgel scaffolds can support spatial osteochondral differentiation through discrete presentation of biochemical and mechanical cues. [9, 20] However, these systems inherently rely on step changes in material properties that introduce interfacial discontinuities and potential stress concentrations. The microgel gradient strategy presented here enables spatial mechanical patterning within a single material system, which may reduce interfacial discontinuities while maintaining macroporosity and cell permissiveness. Direct experimental comparisons between continuous and biphasic architectures were outside the scope of the present study but represent an important direction for future work.

These findings position photoannealed microgel gradients as a controlled *in vitro* system for probing mechanobiology and spatial regulation of MSC behavior through mechanical features relevant to the osteochondral unit while addressing limitations inherent to layered scaffolds. [36, 37] Importantly, temporal mechanical characterization demonstrated that the photopatterned stiffness gradient remained stable over the 21-day culture period. Bulk compressive modulus, swelling ratio, and dry mass measurements all remained unchanged, indicating stable polymer content and hydration of the PEG network. While the maximum modulus measured by nanoindentation was modestly reduced at Day 21 relative to Day 1, the spatial gradient profile and architecture-dependent ordering of scaffold stiffness were preserved. This decrease may reflect hydrogel equilibration during culture rather than degradation of the PEG network, as PEG-VS covalently crosslinked with PEG-DT lacks degradable linkers under the culture conditions used here. Because all microgel populations were fabricated from the same PEG-VS/PEG-DT chemistry and crosslinking scheme, differences in microgel diameter are therefore expected to alter scaffold architecture rather than intrinsic hydrogel degradation behavior. Continuous transitions in stiffness allow MSCs to adopt region-appropriate phenotypes in response to endogenous mechanical cues, producing spatial patterns of proteoglycan-rich and mineralized

matrix that resemble early cartilage and bone zones. [28, 38] This single-material strategy represents an advance over multiphasic constructs that depend on abrupt interfaces or exogenous biochemical patterning to control cell behavior. [39, 40] By integrating microgel-derived porosity with a tunable modulus gradient, the system enables matrix transport, cell infiltration, and local mechanotransduction to operate concurrently to attain coordinated osteochondral repair. [5, 8] These findings align with emerging views that successful osteochondral regeneration requires scaffolds that guide cells through spatially organized mechanical environments rather than relying solely on exogenous growth factors or layered architectures. [41] The ability to couple mechanical gradients with controlled pore geometry offers opportunities to probe how MSCs integrate multiscale physical signals and to design constructs that support spatial tissue assembly without relying on specialized manufacturing steps or spatial delivery of growth factors. [42] Such modularity provides a foundation for future work that tailors gradient strength, microgel chemistry, or dynamic loading to guide more mature osteochondral tissue formation.

Taken together, these results support the conclusion that continuous mechanical gradients within a macroporous microgel scaffold are sufficient to regulate spatially organized MSC responses associated with osteochondral differentiation. Several limitations nevertheless warrant consideration. We examined MSC behavior using MSCs from a single donor, one PEG-VS/PEG-DT formulation, and a mixed osteochondral medium; therefore, responses may differ with additional donors, alternative hydrogel chemistries, or more defined chondrogenic and osteogenic cue presentation. Future studies incorporating multiple MSC donors, degradable or ECM-interactive microgel chemistries, and lineage-specific media will be important to assess robustness and donor-dependent variability. We focused on a single stiffness range and gradient strength selected to span a broad osteochondral-relevant modulus range and did not systematically vary gradient magnitude, spatial length scale, or temporal presentation. Accordingly, these studies should be interpreted as a proof-of-concept demonstration of spatial

stiffness regulation within a granular scaffold rather than a systematic optimization of gradient steepness, modulus ranges, or microgel size combinations. Furthermore, the present work did not directly compare continuous gradients with discrete biphasic scaffold architectures, which could provide additional insight into how mechanical continuity influences MSC patterning. Systematic modulation of gradient steepness, absolute modulus range, and dynamic gradient evolution enabled by staged photoannealing or degradable crosslinks would reveal a broader understanding of how mechanical parameters govern spatial patterning and lineage commitment. Our mechanobiologic readouts relied on cytoskeletal imaging and endpoint expression of the YAP/TAZ-associated target gene *CTGF* rather than direct interrogation of upstream signaling. Future work integrating spatially resolved molecular analyses, including YAP/TAZ nuclear localization, integrin signaling, focal adhesion composition, and protein-level pathway activation across the gradient, will provide deeper mechanistic insight into how cells interpret multiscale physical cues. Finally, constructs were evaluated at a fixed volume over 21 days under static culture conditions without dynamic mechanical loading. In native osteochondral tissue, cells are exposed to cyclic compressive and shear forces generated during joint motion, which regulate mesenchymal stromal cell mechanotransduction pathways, matrix deposition, and tissue maturation. [43, 44] Static culture was intentionally used here to isolate the effects of spatial stiffness gradients and scaffold architecture on MSC behavior without introducing additional mechanical variables. Accordingly, this study was designed as a mechanistic *in vitro* model to isolate the effects of spatial stiffness gradients on MSC behavior rather than to evaluate osteochondral repair efficacy *in vivo*. Nevertheless, acellular mechanical measurements confirmed that the spatial stiffness gradient remained stable throughout the 21-day culture period. Static culture conditions were intentionally employed in this study to isolate the effects of spatially organized stiffness on MSC behavior within a controlled three-dimensional microenvironment.

While native osteochondral tissues are subject to dynamic compressive and shear loading, which are known to regulate mechanotransduction, matrix synthesis, and tissue maturation, incorporation of additional stimuli introduces variables that can confound interpretation of stiffness-driven effects. [43, 45] As such, this system is designed as a simplified platform to decouple mechanical cues arising from scaffold architecture from externally applied forces. Future studies will incorporate dynamic mechanical loading, including cyclic compression and shear, to evaluate how these factors interact with spatial stiffness gradients to further regulate osteochondral tissue formation. As an *in vitro* system, this study does not capture the full complexity of the *in vivo* osteochondral environment, including immune response, scaffold integration, mechanical loading, degradation kinetics, and long-term functional repair. While the present findings demonstrate that spatial stiffness gradients regulate MSC behavior within a controlled microenvironment, *in vivo* validation in osteochondral defect models will be necessary to determine the capacity of this platform to support spatial tissue regeneration, host integration, and functional repair outcomes. Future studies incorporating physiologic loading regimens as well as *in vivo* implantation, will be important to determine how externally applied mechanical forces interact with scaffold stiffness gradients to regulate long-term tissue organization, integration, and translational potential of this microgel gradient platform. Future studies should also directly compare continuous gradient scaffolds and biphasic scaffolds to evaluate differences in interfacial stress distribution, matrix organization, and functional tissue outcomes.

Conclusion

This study establishes a hydrogel scaffold possessing a controllable stiffness gradient with macroporous architecture. Smaller microgels, which generate tighter void networks and greater interfacial surface area, produced distinct regional differences in cell behavior, matrix deposition,

and osteochondral gene expression, demonstrating the combined influence of stiffness and pore architecture on local cell–matrix interactions. These findings position photoannealed microgel gradients as a versatile system for probing mechanobiology and guiding zonal tissue formation. Future studies incorporating *in vivo* osteochondral defect models will be necessary to determine the capacity of this platform to support spatial tissue regeneration, host integration, and long-term functional repair. By pairing spatially resolved mechanics with tunable microstructural design, this approach offers a single-material strategy to promote organized osteochondral regeneration without external patterning or layered scaffold architectures. Future work will integrate dynamic mechanical stimulation to evaluate the combined effects of scaffold architecture and physiologic loading on MSC differentiation and tissue formation. Studies incorporating *in vivo* osteochondral defect models will be necessary to evaluate the translational potential of this platform and its ability to support functional tissue regeneration.

Competing interests

The authors declare they do not have any competing interests.

Data and materials availability

The dataset generated and/or analyzed during the current study are available from the corresponding authors upon reasonable request.

Acknowledgements

Research reported in this publication was supported by the National Institute of Dental and Craniofacial Research of the National Institutes of Health under award numbers R01 DE025899 and R01 AR079211. SCM was supported by a UC-National Lab In-Residence Graduate

Fellowship (L23GF6290) and a National Institute of Arthritis and Musculoskeletal and Skin Diseases funded training program in Musculoskeletal Health Research (T32 AR079099). This work was performed under the auspices of the US Department of Energy by Lawrence Livermore National Laboratory under Contract DE-AC52-07NA27344. Information release number LLNL-JRNL-2015142. The funders had no role in the decision to publish, or preparation of the manuscript. JKL also acknowledges financial support from the Lawrence J. Ellison Endowed Chair of Musculoskeletal Research. Generative AI tools were used for limited language editing only.

Supplementary Figures for

Mechanically Graded Granular Scaffolds for Osteochondral Tissue Engineering

Sabrina C. Mierswa[1,2,3], Erika E. Wheeler[1,2], Monica L. Moya[3], and J. Kent Leach[1,2]

[1] Department of Orthopaedic Surgery, UC Davis Health, Sacramento, CA, 95817, USA
[2] Department of Biomedical Engineering, University of California, Davis, CA, 95616, USA
[3] Engineering Directorate, Lawrence Livermore National Laboratory, Livermore, CA, USA

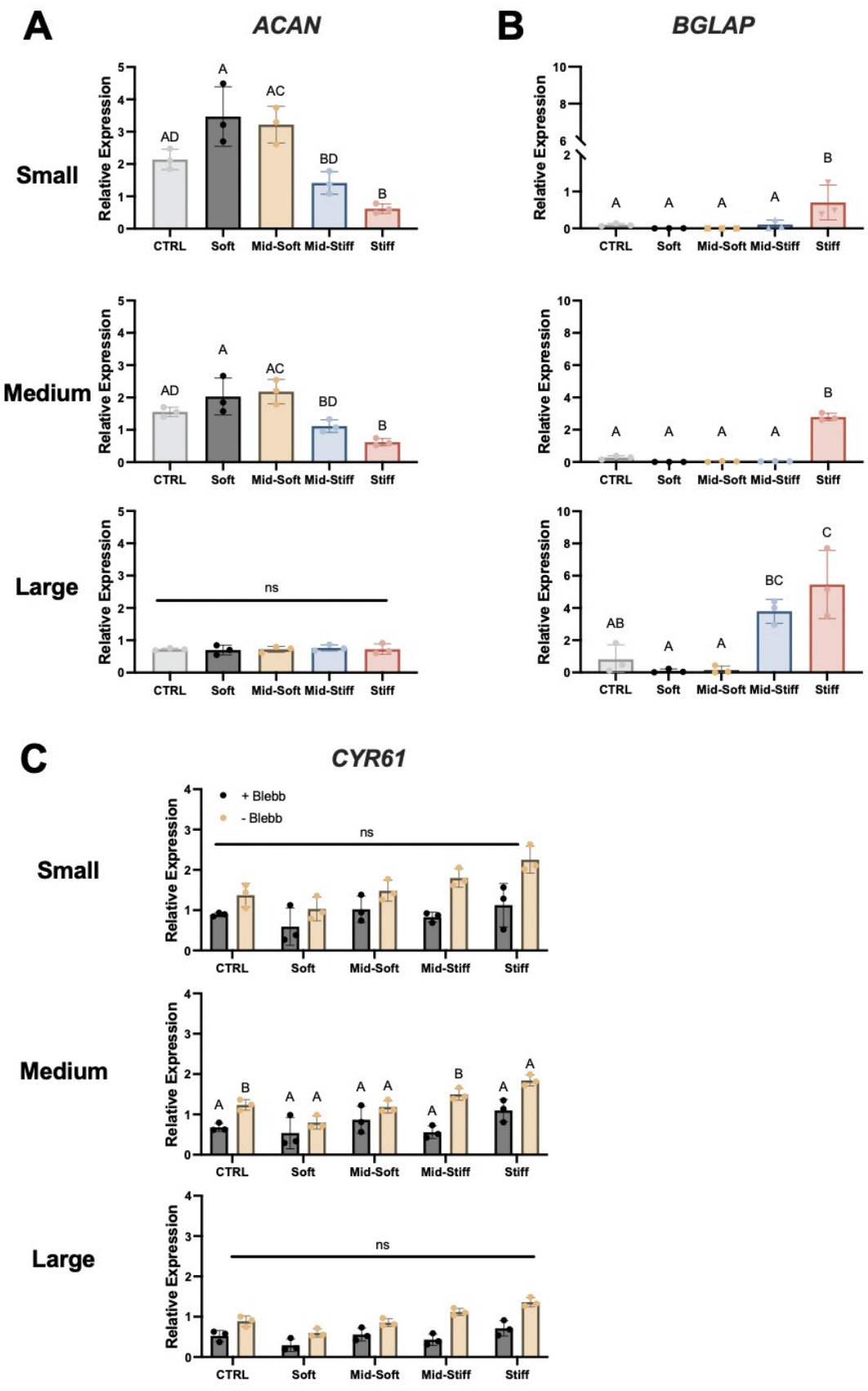
A
ACAN
B
BGLAP
Small
Medium
Large
Relative Expression
CTRL
Soft
Mid-Soft
Mid-Stiff
Stiff
AD
A
AC
BD
B
ns
AB
BC
C
C
CYR61
+ Blebb
- Blebb

Figure S1. Stiffness gradient–dependent regulation of chondrogenic and osteogenic gene expression across microgel architectures. (**A**) Relative expression of the chondrogenic marker *ACAN* in MSCs cultured within stiffness gradient scaffolds assembled from small, medium, or large microgels. (**B**) Relative expression of the osteogenic marker *BGLAP* across stiffness gradient regions for small, medium, and large microgel scaffolds. (**C**) Relative expression of the mechanosensitive gene *CYR61* in stiffness gradient scaffolds treated with blebbistatin (+Blebb) or untreated (–Blebb). Data are presented as mean ± SD (n = 3 constructs per region). Statistical significance was determined using a Student's t-test or one-way ANOVA with Tukey's multiple comparisons test where appropriate. Groups that do not share a letter are significantly different ($p < 0.05$); ns = not significant.

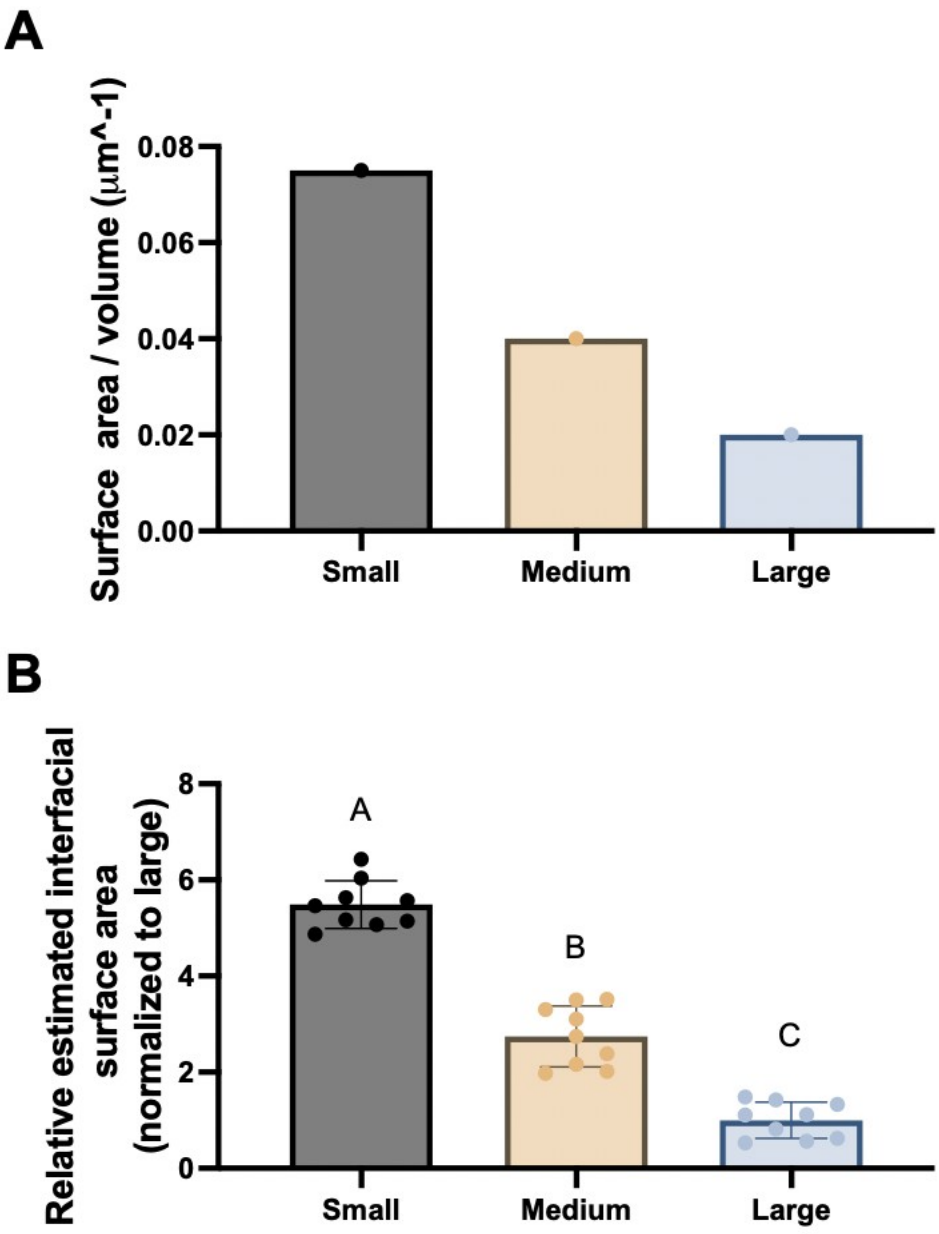

Figure S2. Geometric scaling of microgel architecture and estimated scaffold interfacial surface area. (**A**) Surface area-to-volume ratio of individual spherical microgels calculated from measured microgel diameters for small, medium, and large microgel formulations. Values represent calculated geometric relationships increasing the increase in surface area relative to volume with decreasing microgel diameter. (**B**) Relative estimated scaffold interfacial surface area derived from experimentally measured scaffold porosity and microgel radius for small, medium,

and large microgel scaffolds. Values are normalized to the mean large-microgel condition. Data are presented as mean ± SD (n = 9 measurements per condition). Statistical significance was determined using one-way ANOVA with Tukey's multiple comparisons test where appropriate. Groups that do not share a letter are significantly different ($p < 0.05$); ns = not significant.

References

1. Armiento AR, Stoddart MJ, Alini M, Eglin D. Biomaterials for articular cartilage tissue engineering: Learning from biology. Acta Biomater. 2018;65:1–20.
2. Makris EA, Gomoll AH, Malizos KN, Hu JC, Athanasiou KA. Repair and tissue engineering techniques for articular cartilage. Nat Rev Rheumatol. 2015;11(1):21–34.
3. Huey DJ, Hu JC, Athanasiou KA. Unlike bone, cartilage regeneration remains elusive. Science. 2012;338(6109):917–21.
4. Nooeaid P, Salih V, Beier JP, Boccaccini AR. Osteochondral tissue engineering: scaffolds, stem cells and applications. J Cell Mol Med. 2012;16(10):2247–70.
5. Nordberg RC, Wen DH, Wang D, Hu JC, Athanasiou KA. Challenges and recent advances in engineering the osteochondral interface. Curr Opin Biomed Eng. 2024;31.
6. Yu L, Cavelier S, Hannon B, Wei M. Recent development in multizonal scaffolds for osteochondral regeneration. Bioact Mater. 2023;25:122–59.
7. Choe R, Devoy E, Jabari E, Packer JD, Fisher JP. Biomechanical aspects of osteochondral regeneration: Implications and strategies for three-dimensional bioprinting. Tissue Eng Part B Rev. 2022;28(4):766–88.
8. Niu X, Li N, Du Z, Li X. Integrated gradient tissue-engineered osteochondral scaffolds: Challenges, current efforts and future perspectives. Bioact Mater. 2023;20:574–97.
9. Lowen JM, Wheeler EE, Shimamoto NK, Ramos-Rodriguez DH, Griffin KH, Bond GC, et al. Functionalized annealed microgels for spatial control of osteogenic and chondrogenic differentiation. Adv Funct Mater. 2024;34(30):2311017.
10. Steinmetz NJ, Aisenbrey EA, Westbrook KK, Qi HJ, Bryant SJ. Mechanical loading regulates human MSC differentiation in a multi-layer hydrogel for osteochondral tissue engineering. Acta Biomater. 2015;21:142–53.
11. Schek RM, Taboas JM, Segvich SJ, Hollister SJ, Krebsbach PH. Engineered osteochondral grafts using biphasic composite solid free-form fabricated scaffolds. Tissue Eng. 2004;10(9-10):1376–85.
12. Xia T, Liu W, Yang L. A review of gradient stiffness hydrogels used in tissue engineering and regenerative medicine. J Biomed Mater Res A. 2017;105(6):1799–812.
13. Mierswa SC, Wheeler EE, Apsey AN, Jeon O, Alsberg E, Leach JK. Mesenchymal stromal cell chondrogenic differentiation induced by continuous stiffness gradient in photocrosslinkable hydrogels. J Biomed Mater Res A. 2025;113(5):e37928.
14. Tse JR, Engler AJ. Stiffness gradients mimicking in vivo tissue variation regulate mesenchymal stem cell fate. PLoS One. 2011;6(1):e15978.
15. Kloxin AM, Kasko AM, Salinas CN, Anseth KS. Photodegradable hydrogels for dynamic tuning of physical and chemical properties. Science. 2009;324(5923):59–63.
16. Griffin DR, Weaver WM, Scumpia PO, Di Carlo D, Segura T. Accelerated wound healing by injectable microporous gel scaffolds assembled from annealed building blocks. Nat Mater. 2015;14(7):737–44.
17. Qazi TH, Mooney DJ, Duda GN, Geissler S. Biomaterials that promote cell-cell interactions enhance the paracrine function of MSCs. Biomaterials. 2017;140:103–14.
18. Daly AC, Critchley SE, Rencsok EM, Kelly DJ. A comparison of different bioinks for 3D bioprinting of fibrocartilage and hyaline cartilage. Biofabrication. 2016;8(4):045002.
19. Chen J, Li Q, Li H, Lv C, Yu H, Feng Q, et al. Injectable acellular matrix microgel assembly with stem cell recruitment and chondrogenic differentiation functions promotes microfracture-based articular cartilage regeneration. Bioact Mater. 2025;44:220–35.

20. Chi M, Zheng X, Zhang F, Xuan Z, Tang X, Zhang J, et al. Self-assembled porous microgel scaffold with layered drug release for efficient repair of osteochondral microstructure. Biomater Adv. 2025;177:214402.
21. Lowen JM, Bond GC, Griffin KH, Shimamoto NK, Thai VL, Leach JK. Multisized photoannealable microgels regulate cell spreading, aggregation, and macrophage phenotype through microporous void space. Adv Healthc Mater. 2023;12(13):e2202239.
22. Wheeler EE, Apsey AN, Leach JK. Zwitterionic Microgel Scaffolds Support Matrix Accumulation by Regulating Protein Adsorption. Adv Healthc Mater. 2025:e03483.
23. de Rutte JM, Koh J, Di Carlo D. Scalable high-throughput production of modular microgels for in situ assembly of microporous tissue scaffolds. Adv Funct Mater. 2019;29(25).
24. Hung BP, Harvestine JN, Saiz AM, Gonzalez-Fernandez T, Sahar DE, Weiss ML, et al. Defining hydrogel properties to instruct lineage- and cell-specific mesenchymal differentiation. Biomaterials. 2019;189:1–10.
25. Bril M, Saberi A, Jorba I, van Turnhout MC, Sahlgren CM, Bouten CVC, et al. Shape-morphing photoresponsive hydrogels reveal dynamic topographical conditioning of fibroblasts. Adv Sci (Weinh). 2023;10(31):e2303136.
26. Piazza F, Parisse P, Passerino J, Marsich E, Bersanini L, Porrelli D, et al. Controlled quenching of agarose defines hydrogels with tunable structural, bulk mechanical, surface nanomechanical, and cell response in 2D cultures. Adv Healthc Mater. 2023;12(26):e2300973.
27. Jaberi A, Kedzierski A, Kheirabadi S, Tagay Y, Ataie Z, Zavari S, et al. Engineering microgel packing to tailor the physical and biological properties of gelatin methacryloyl granular hydrogel scaffolds. Adv Healthc Mater. 2024;13(25):e2402489.
28. Elosegui-Artola A, Oria R, Chen Y, Kosmalska A, Perez-Gonzalez C, Castro N, et al. Mechanical regulation of a molecular clutch defines force transmission and transduction in response to matrix rigidity. Nat Cell Biol. 2016;18(5):540–8.
29. Ranga A, Gobaa S, Okawa Y, Mosiewicz K, Negro A, Lutolf MP. 3D niche microarrays for systems-level analyses of cell fate. Nat Commun. 2014;5:4324.
30. Das RK, Gocheva V, Hammink R, Zouani OF, Rowan AE. Stress-stiffening-mediated stem-cell commitment switch in soft responsive hydrogels. Nat Mater. 2016;15(3):318–25.
31. Gonzalez-Fernandez T, Tenorio AJ, Saiz AM, Jr., Leach JK. Engineered cell-secreted extracellular matrix modulates cell spheroid mechanosensing and amplifies their response to inductive cues for the formation of mineralized tissues. Adv Healthc Mater. 2022;11(10):e2102337.
32. Dupont S, Morsut L, Aragona M, Enzo E, Giulitti S, Cordenonsi M, et al. Role of YAP/TAZ in mechanotransduction. Nature. 2011;474(7350):179–83.
33. McDermott AM, Eastburn EA, Kelly DJ, Boerckel JD. Effects of chondrogenic priming duration on mechanoregulation of engineered cartilage. J Biomech. 2021;125:110580.
34. Steinwachs J, Metzner C, Skodzek K, Lang N, Thievessen I, Mark C, et al. Three-dimensional force microscopy of cells in biopolymer networks. Nat Methods. 2016;13(2):171–6.
35. Murphy CM, Haugh MG, O'Brien FJ. The effect of mean pore size on cell attachment, proliferation and migration in collagen-glycosaminoglycan scaffolds for bone tissue engineering. Biomaterials. 2010;31(3):461–6.
36. Sharma B, Williams CG, Kim TK, Sun D, Malik A, Khan M, et al. Designing zonal organization into tissue-engineered cartilage. Tissue Eng. 2007;13(2):405–14.
37. Zhang L, Dai W, Gao C, Wei W, Huang R, Zhang X, et al. Multileveled hierarchical hydrogel with continuous biophysical and biochemical gradients for enhanced repair of full-thickness osteochondral defect. Adv Mater. 2023;35(19):e2209565.
38. Chaudhuri O, Gu L, Klumpers D, Darnell M, Bencherif SA, Weaver JC, et al. Hydrogels with tunable stress relaxation regulate stem cell fate and activity. Nat Mater. 2016;15(3):326–34.

39. Sherwood JK, Riley SL, Palazzolo R, Brown SC, Monkhouse DC, Coates M, et al. A three-dimensional osteochondral composite scaffold for articular cartilage repair. Biomaterials. 2002;23(24):4739–51.
40. Lynn AK, Best SM, Cameron RE, Harley BA, Yannas IV, Gibson LJ, et al. Design of a multiphase osteochondral scaffold. I. Control of chemical composition. J Biomed Mater Res A. 2010;92(3):1057–65.
41. Bian L, Guvendiren M, Mauck RL, Burdick JA. Hydrogels that mimic developmentally relevant matrix and N-cadherin interactions enhance MSC chondrogenesis. Proc Natl Acad Sci U S A. 2013;110(25):10117–22.
42. Trappmann B, Gautrot JE, Connelly JT, Strange DG, Li Y, Oyen ML, et al. Extracellular-matrix tethering regulates stem-cell fate. Nat Mater. 2012;11(7):642–9.
43. Engler AJ, Sen S, Sweeney HL, Discher DE. Matrix elasticity directs stem cell lineage specification. Cell. 2006;126(4):677–89.
44. Thorpe SD, Buckley CT, Vinardell T, O'Brien FJ, Campbell VA, Kelly DJ. The response of bone marrow-derived mesenchymal stem cells to dynamic compression following TGF-beta3 induced chondrogenic differentiation. Ann Biomed Eng. 2010;38(9):2896–909.
45. Discher DE, Janmey P, Wang YL. Tissue cells feel and respond to the stiffness of their substrate. Science. 2005;310(5751):1139–43.